JOURNAL OF MAGNETIC RESONANCE, Series B 103, 203–216 (1994)

Gradient-Enhanced Triple-Resonance Three-Dimensional NMR Experiments with Improved Sensitivity

D. R. MUHANDIRAM AND LEWIS E. KAY

Protein Engineering Network Centers of Excellence and Departments of Medical Genetics, Biochemistry and Chemistry, University of Toronto, Toronto, Ontario, Canada M5S 1A8

Received February 22, 1993; revised May 18, 1993

The sensitivities of a number of gradient and nongradient versions of triple-resonance experiments are compared by quantitating the signal-to-noise ratios in spectra recorded on *Cellulomonas fimi* cellulose binding domain (110 amino acids), *Xenopus laevis* calmodulin (148 amino acids), *Mycococcus xanthus* protein S (173 amino acids), and a 93-amino acid fragment of protein S. It is shown that it is possible to construct sensitivity-enhanced gradient experiments, with ^{15}N selection achieved via pulsed field gradients, that are as sensitive as their sensitivity-enhanced nongradient counterparts and significantly more sensitive than other gradient approaches. These sequences are very closely related to the family of improved-sensitivity sequences proposed by Rance and co-workers (A. G. Palmer, J. Cavanagh, P. E. Wright, and M. Rance, *J. Magn. Reson.* 93, 151, 1991). The use of gradients greatly improves the quality of water suppression and reduces both the number of artifacts and the phase-cycling requirements at no cost in sensitivity for the proteins considered in this study.

INTRODUCTION

It has long been recognized that the use of pulsed field gradients allows the selection of NMR signals having certain desired properties and the elimination of artifacts that are often difficult to suppress with nongradient methods (*1, 2*). However, the incorporation of pulsed field gradients in a large number of high-resolution NMR experiments had to await the recent advances in gradient technology such as the development of actively shielded gradients. The advantages of the use of gradients in NMR experiments include a reduction in the number of phase-cycling steps for the suppression of experimental artifacts, a decrease in experiment acquisition times for sufficiently concentrated samples, a reduction in t_1 noise, and efficient suppression of the intense solvent signal in H_2O samples (*3–7*). In addition to decreasing the dynamic-range problem, efficient suppression of the intense water signal with gradients allows the recording of many of the experiments normally reserved for D_2O samples on samples dissolved in H_2O (*8*). This offers significant advantages in triple-resonance experiments for backbone assignment of $^{15}N, ^{13}C$-labeled proteins in that the use of a single sample (H_2O) eliminates ambiguities in comparing chemical shifts from spectra recorded on H_2O and D_2O samples.

Recently approaches have been developed in a number of different laboratories for recording pure-absorption spectra where coherence-transfer selection is achieved through the use of gradients (*9–11*). This advance is significant for biomolecular applications since in many instances resolution is often limiting. The disadvantage of many of these experiments, however, is the loss in sensitivity that is obtained relative to nongradient experiments due to the fact that N- or P-type coherence pathways, but not both, are selected during a single scan.

In a recent publication, we described a pure-absorption $^1H-^{15}N$ HSQC experiment with coherence-transfer selection achieved via gradient pulses, which offers substantial improvements in sensitivity over experiments recorded with other gradient schemes (*12*). This experiment is very closely related to an elegant set of nongradient pulse sequences developed by Rance and co-workers which gives enhanced sensitivity (*13–15*). In the present work, enhanced-sensitivity $^{15}N, ^{13}C$ gradient three-dimensional triple-resonance experiments with NH detection are presented where the gradients are used to select the coherence-transfer pathway which involves magnetization passing through ^{15}N. In particular, the pulse scheme of the enhanced-sensitivity gradient HNCO experiment is discussed in detail and compared with several other gradient and nongradient triple-resonance HNCO pulse sequences. A theoretical analysis of the expected sensitivities of each of the experiments is presented. Experimental verification of the results presented under Theory is provided by recording spectra on a number of different protein samples: the cellulose binding domain fragment of a cellulase from *Cellulomonas fimi* (CBD; a dimer consisting of monomers of 110 amino acids), *Xenopus laevis* calmodulin (148 amino acids), *Myxococcus xanthus* protein S (173 amino acids), and a 93-amino acid fragment of protein S. It is shown that the enhanced gradient HNCO experiment is as sensitive as its enhanced nongradient counterpart and significantly

1064-1866/94 $6.00

more sensitive than HNCO experiments recorded with other gradient approaches. Finally, we conclude by illustrating (i) an enhanced gradient version of the CBCA(CO)NH experiment (*16*) which links ^{15}N and NH shifts with Cβ and Cα shifts of the preceding residue and (ii) an enhanced gradient version of the HNCACB experiment (*17*) which links the intraresidue ^{15}N, NH, Cβ, and Cα shifts and, in addition, provides connectivities between the ^{15}N and NH shifts and Cβ and Cα shifts of the previous residue. We have found that the combined use of these two experiments offers an extremely powerful approach for sequential backbone assignment of ^{15}N,^{13}C-labeled proteins, and that for proteins giving reasonably well-dispersed spectra, often the information content in these two experiments is sufficient for the complete sequential assignment.

THEORY

The sensitivity gains associated with the improved-sensitivity versions of the pulsed field gradient triple-resonance experiments can be readily appreciated by comparing a number of different schemes for recording triple-resonance experiments. In this section, the relative sensitivities of a number of gradient and nongradient versions of the HNCO experiment (*18, 19*) are calculated. Although attention is focused on the HNCO experiment, similar conclusions will hold for other triple-resonance experiments in which NH protons are detected. The detailed mechanism of magnetization transfer in the HNCO experiment has been discussed in detail elsewhere (*19, 20*) and will not be repeated completely here. Briefly, the magnetization-transfer pathway is

$$\mathrm{NH} \xrightarrow{J_{NH}} {}^{15}\mathrm{N} \xrightarrow{J_{NC'}} {}^{13}\mathrm{C}'(t_1) \xrightarrow{J_{NC'}} {}^{15}\mathrm{N}(t_2) \xrightarrow{J_{NH}} \mathrm{NH}(t_3),$$

where the active couplings involved in each transfer process are indicated above each arrow and t_i (i = 1–3) indicates that magnetization is acquired during this time. In particular, J_{NH} and $J_{NC'}$ are the one-bond ^{15}N–NH and ^{15}N–C′ (C′ = carbonyl) couplings.

Figures 1a–1e illustrate the HNCO sequences that are considered. The sequence in Fig. 1a is essentially the constant-time refocused HNCO experiment of Grzesiek and Bax (*20*) with the exception that the ^{15}N chemical shift is recorded following the C′ evolution period. In Fig. 1b, a gradient version of the HNCO experiment is presented, where the gradients are employed to select for a particular coherence-transfer pathway. The use of gradients in this experiment is analogous to their use in a gradient HNCO pulse scheme recently proposed by Davis *et al.* (*21*). In Fig. 1c, gradients are employed to select for either N-type or P-type signals. By alternating the relative sign of the last two gradients in the sequence, g3 and g4, it is possible to record pure-absorption data sets (*9–11*). Figure 1d illustrates the sensitivity-enhanced pulsed field gradient HNCO experiment. In this case, g3 and g8 are used to select the desired coherence-transfer pathway. In Fig. 1e, an enhanced, nongradient version of the HNCO experiment (the nongradient counterpart of the sequence in Fig. 1d) is presented for comparison.

In what follows, a product-operator description (*22*) of each of the sequences is provided. Because each of the pulse schemes is essentially the same up to the ^{15}N evolution, the description of each of the experiments starts immediately after the application of the ^{15}N 90° pulse of phase ϕ_4 (point a in each of the sequences). The symbols I, N, and C′ denote NH, ^{15}N, and $^{13}C'$ magnetization, respectively. The effects of relaxation are initially ignored; the phases of all pulses are as indicated in the first line of the phase cycle described in the legend to Fig. 1 or else explicitly indicated during the derivation. For simplicity, the values of τ_a, τ_b, and τ_c are assumed equal to $1/(4J_{NH})$, $1/(2J_{NH})$, and $1/(4J_{NH})$, respectively. In the gradient sequences, the shaded gradients are those gradients used to select for a particular coherence-transfer pathway. It is assumed throughout that these gradients are applied with sufficient strength that transverse magnetization is completely randomized and that refocusing of magnetization occurs only when the net phase imparted to the magnetization by the gradients is zero. In contrast, the other gradients are inserted to aid in the suppression of artifacts caused by pulse imperfections (*23*). All gradients are in the z direction.

Sequence a. The density operator at point a in Fig. 1a, for $\phi_4 = x$, can be written as

$$\rho_a = -2N_yC'_z, \qquad [1]$$

where N_y and C'_z denote the y and z components of ^{15}N and carbonyl magnetization, respectively. At the end of the constant-time ^{15}N evolution period (point b), the magnetization of interest can be described by

$$\rho_b = 2N_yI_z\cos(\omega_N t_2)\sin(2\pi J_{NC'}T), \qquad [2]$$

where ω_N is the ^{15}N Larmor frequency. The evolution of magnetization during $2T$ due to ^{15}N–$^{13}C\alpha$ couplings is suppressed by SEDUCE-1 decoupling (*24, 25*) of the $^{13}C\alpha$ spins.

Immediately prior to acquisition, the magnetization is given by

$$\rho_c = I_x\cos(\omega_N t_2)\sin(2\pi J_{NC'}T). \qquad [3]$$

Quadrature in the ^{15}N dimension is obtained according to the recipe of States *et al.* (*26*) by recording spectra with $\phi_4 = x, y$ for each t_2 value and storing the resultant FIDs separately. A calculation analogous to that given above shows

that for $\phi_4 = y$, the magnetization immediately prior to acquisition is given by

$$\rho_c = I_x \sin(\omega_N t_2)\sin(2\pi J_{NC'} T). \quad [4]$$

Sequence b. The density operator at point a in Fig. 1b, for $\phi_4 = x$, can be written as

$$\rho_a = -2\alpha N_y C'_z, \quad [5]$$

where $\alpha = 0.5\{\exp(i\theta_1) + \exp(-i\theta_1)\}$ and $\theta_1 = \gamma_N B_1(z)\tau_1$, where γ_N is the gyromagnetic ratio of the ^{15}N spin, $B_1(z)$ is the z-dependent magnetic field generated by the gradient, and τ_1 is the duration of the gradient pulse. The factor α arises due to the application of gradient pulse g3 during the T_N period. At b in the sequence, the magnetization is given by

$$\rho_b = 2N_y I_z \alpha \cos(\omega_N t_2)\sin(2\pi J_{NC'} T). \quad [6]$$

Immediately prior to detection, the signal of interest can be described by

$$\rho_c = (1/4)A\{I_+\exp[i(\theta_1 + \theta_2)] + I_+\exp[-i(\theta_1 - \theta_2)] + I_-\exp[i(\theta_1 - \theta_2)] + I_-\exp[-i(\theta_1 + \theta_2)]\}, \quad [7]$$

where $A = \cos(\omega_N t_2)\sin(2\pi J_{NC'} T)$, $\theta_2 = \gamma_H B_2(z)\tau_2$. The symbol γ_H is the gyromagnetic ratio of the proton spin, $B_2(z)$ is the z-dependent magnetic field generated by this gradient (g4), τ_2 is the duration of the gradient pulse, $I_\pm = I_x \pm iI_y$, and θ_1 is defined previously. If the strengths and durations of the gradients used to select for ^{15}N magnetization (g3 and g4) are adjusted to satisfy the condition

$$\gamma_N B_1(z)\tau_1 = \pm\gamma_H B_2(z)\tau_2, \quad [8]$$

then only those terms proportional to $\exp[\pm i(\theta_1 + \theta_2)]$ $[\gamma_N B_1(z)\tau_1 = -\gamma_H B_2(z)\tau_2]$ or $\exp[\pm i(\theta_1 - \theta_2)]$ $[\gamma_N B_1(z)\tau_1 = \gamma_H B_2(z)\tau_2]$ but not both will contribute to observed magnetization. Equation [7] becomes

$$\rho_c = 0.5 I_x \cos(\omega_N t_2)\sin(2\pi J_{NC'} T). \quad [9]$$

When $\phi_4 = y$, a calculation similar to that given above shows that the signal immediately prior to detection is given by

$$\rho_c = 0.5 I_x \sin(\omega_N t_2)\sin(2\pi J_{NC'} T). \quad [10]$$

A comparison of Eqs. [3] and [4] and Eqs. [9] and [10] shows that by selecting for ^{15}N magnetization using this approach, the signal is reduced by a factor of 2 relative to that in the nongradient approach. Note that in this experiment, quadrature in the ^{15}N dimension is obtained by the usual States method (*26*).

Sequence c. At position a in Fig. 1c, the magnetization is given by

$$\rho_a = -2N_y C'_z, \quad [11]$$

while at b the density operator of interest is

$$\rho_b = -(i/2)\sin(2\pi J_{NC'} T) \times \{2N_+ I_z \exp(-i\theta_1) - 2N_- I_z \exp(i\theta_1)\}, \quad [12]$$

where $N_\pm = N_x \pm iN_y$ and $\theta_1 = \omega_N t_2 - \gamma_N B_1(z)\tau_1$. The ^{13}C$\alpha$ decoupling during the $2T$ period is terminated immediately prior to the application of gradient pulse g3, since as described later, the application of gradient pulses during decoupling can interfere with the effects of decoupling, leading to sensitivity losses. The duration of gradient pulse g3 is sufficiently short (2.5 ms) that very little evolution of ^{15}N magnetization due to coupling with ^{13}Cα will occur in this time. If the strength and duration of g4 are chosen to satisfy the condition $\gamma_N B_1(z)\tau_1 = \gamma_H B_2(z)\tau_2$, the signal at the beginning of the acquisition period is given by

$$\rho_c = \sin(2\pi J_{NC'} T) \times \{0.5 I_x \cos(\omega_N t_2) - 0.5 I_y \sin(\omega_N t_2)\}. \quad [13]$$

Equation [13] describes a lineshape that is phase modulated in the ^{15}N dimension. In order to obtain pure-absorption spectra, a separate FID is recorded for each t_2 value where the amplitude of either g3 or g4 (not both) is inverted (*9–11*). This gives a signal of the form

$$\rho_c = \sin(2\pi J_{NC'} T) \times \{0.5 I_x \cos(\omega_N t_2) + 0.5 I_y \sin(\omega_N t_2)\} \quad [14]$$

immediately prior to detection. The signals obtained for the case where the amplitudes of g3 and g4 are of the same and of opposite signs (Eqs. [13] and [14]) are stored in separate memory locations.

Note that, in the sequences in Figs. 1a and 1b, data sets are recorded for $\phi_4 = x, y$ and stored in separate memory locations. In this case, it is the amplitude of g3 or g4 that is inverted and the data obtained are stored separately. The signals obtained for a given t_2 value (and stored in separate memory locations) are added and subtracted in a postacquisition manner (Eq. [13] ± Eq. [14]) and subsequently restored separately. This gives rise to a new data set which can be thought of as originating from ^{15}N amplitude-modulated signals of the form

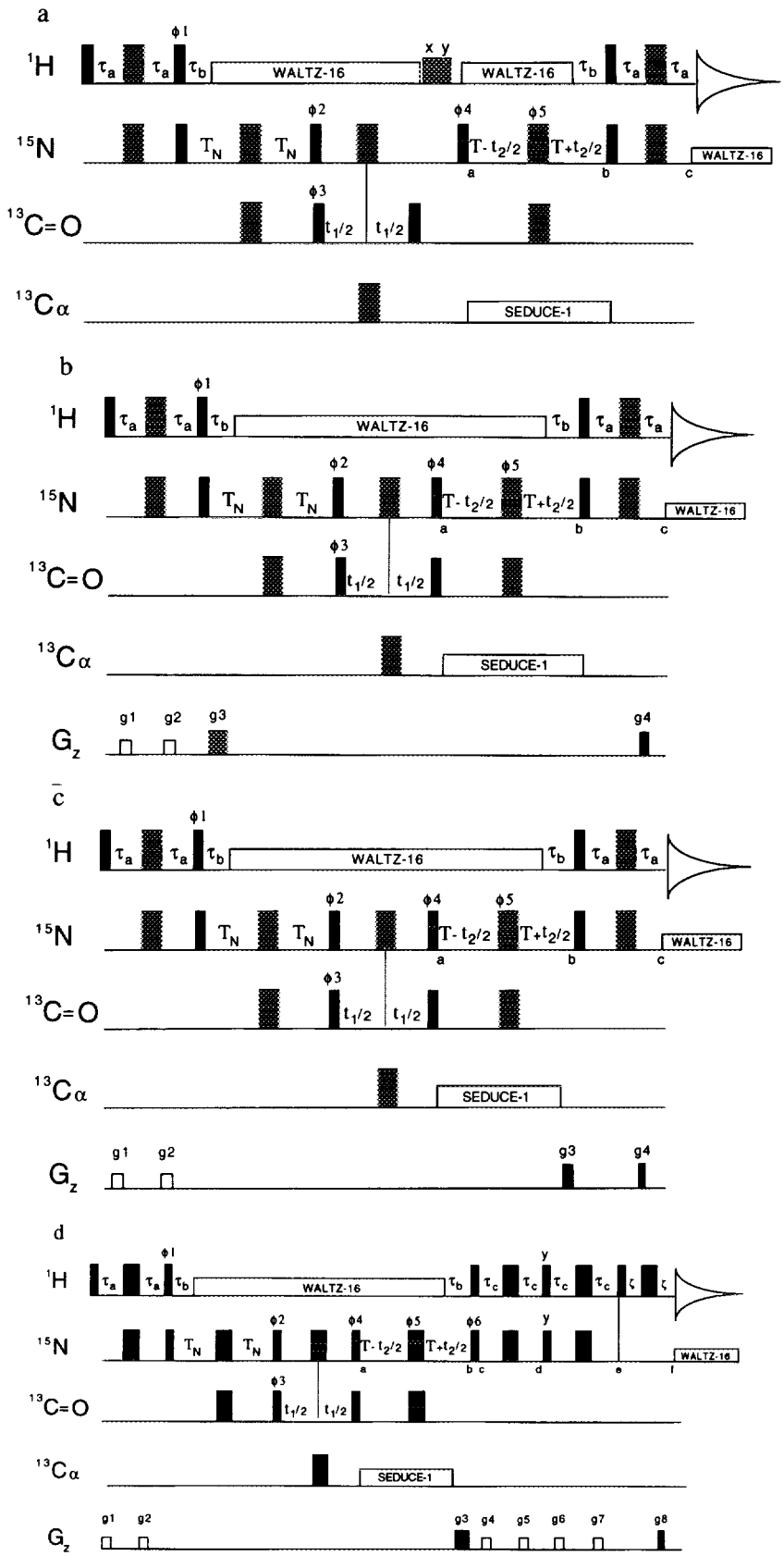
a
^{1}H
^{15}N
^{13}C=O
^{13}Cα
WALTZ-16
SEDUCE-1
b
G$_z$
c
d

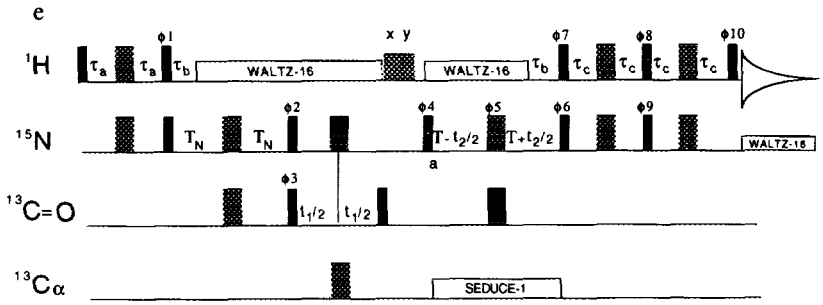

FIG. 1. Several different triple-resonance schemes for recording the HNCO 3D experiment (*18, 19*). In all sequences, the values of τ_a, τ_b, τ_c, T_N, and T are set to 2.3, 5.5, 2.3, 12.4, and 12.4 ms, respectively. WALTZ decoupling (*30*) is achieved using a 6.3 kHz field on the ^{1}H channel and a 1 kHz field on the ^{15}N channel. SEDUCE-1 decoupling (*24, 25*), centered at 54 ppm, using a 825 Hz field ensures that ^{15}N magnetization does not evolve due to scalar coupling to ^{13}Cα during the constant-time t_2 evolution period. All C′ pulses are applied at a field strength of 4.0 kHz so that minimal excitation in the Cα region occurs (*19*). The ^{13}Cα 180° pulse is applied with a field strength of 9.0 kHz, which minimizes the perturbation of the C′ spins. The phase cycling employed for sequences a–d is as follows: $\phi_1 = y, -y$; $\phi_2 = x, -x$; $\phi_3 = 2(x), 2(-x)$; $\phi_4 = x$; $\phi_5 = 4(x), 4(y), 4(-x), 4(-y)$; Acq = $2(x), 4(-x), 2(x)$. (a) Constant-time HNCO scheme of Grzesiek and Bax (*20*), with the exception that ^{15}N acquisition occurs after magnetization is returned from the C′ spins rather than before. Water suppression is achieved with the use of a 10 kHz x purge (6 ms), y purge (3.5 ms) scheme. In the case of presaturation experiments, the water is further suppressed with the use of a 30 Hz field applied for 1 s. Quadrature in t_1 and t_2 is obtained via States–TPPI (*31*) of ϕ_3 and ϕ_4, respectively. (b) Constant-time HNCO experiment with selection of ^{15}N magnetization via gradients applied during nonevolution delays. Water suppression is achieved solely via the gradients. Gradients g1 and g2 are applied for 500 μs at a strength of 5 G/cm, while g3 and g4 are applied for 2.5 and 0.25 ms at strengths of 30 and 29.1 G/cm, respectively. The optimal value of g4 was determined by keeping g3 fixed and maximizing the signal obtained in the first block of the data set. All gradients are rectangular and are applied along the z direction. Quadrature in t_1 and t_2 is obtained as for sequence a. (c) Pulse scheme of the constant-time HNCO experiment with selection of ^{15}N magnetization using a gradient applied during the ^{15}N evolution delay. Water suppression is achieved solely via the gradients. The duration and strengths of the gradients are as for the sequence in b. For each t_2 value, N- and P-type coherences are obtained by recording data sets where the sign of g4 is reversed. Data obtained for positive and negative g4 values (±29.1 G/cm) are stored in separate memory locations, in an analogous manner to the storage of data for $\phi_4 = x, y$ using the method of States (*26*) for sequences a and b. The value of $\phi_4 = x$. Phase ϕ_4 and the receiver phase are inverted for each t_2 increment. Postacquisition processing using home-written software (available upon request) generates pure-absorption data which are subsequently processed in the usual way. (d) Sensitivity-enhanced constant-time HNCO experiment with selection of ^{15}N magnetization using a gradient applied during the ^{15}N evolution delay. All gradients, with the exception of g3 and g8, are applied for 500 μs and at a strength of 5 G/cm. The strengths and durations of g3 and g8 are 30 G/cm, 2.5 ms and ±29.1 G/cm, 0.25 ms, respectively. Water suppression is achieved via the combined action of gradients g3 and g8. For each t_2 value, N- and P-type coherences are obtained by recording data sets where the sign of g8 is reversed. Phase ϕ_6 must also be inverted (from x to $-x$) when the sign of g8 is reversed. Note from Eq. [19] that only a single relative orientation of gradients g3 and g8 will result in refocusing of magnetization for each ϕ_6 value. A determination of the appropriate relative orientation of g3 and g8 for $\phi_6 = x$ and $-x$ is easily accomplished by comparing the signal in the first FID of the experiment for both possibilities. Only in one case should signal be present. Data obtained for positive and negative g8 values are stored in separate memory locations and the generation of pure-absorption lineshapes in the ^{15}N dimension is achieved via postacquisition processing as described previously. The value of ζ is set to 300 μs. The value of this delay must be sufficiently long to ensure that application of the final gradient pulse does not distort the phase or intensity of the spectrum. The value of $\phi_4 = x$. Phase ϕ_4 and the receiver phase are inverted for each t_2 increment. (e) Nongradient sensitivity-enhanced constant-time HNCO experiment. This experiment is very closely related to the family of experiments developed by Rance and co-workers for sensitivity enhancement in a large number of multidimensional NMR experiments (*13–15*). Water suppression is achieved via the use of purge pulses as described for sequence a. For each t_2 value, two data sets are recorded. The first data set is recorded with the phase cycle $\phi_1 = y, -y$; $\phi_2 = x, -x$; $\phi_3 = 2(x), 2(-x)$; $\phi_4 = x$; $\phi_5 = 4(x), 4(y), 4(-x), 4(-y)$; $\phi_6 = 16(x), 16(y)$; $\phi_7 = 16(x), 16(y)$; $\phi_8 = \phi_9 = 16(y), 16(-x)$; $\phi_{10} = 16(x), 16(y)$; Acq = $2(x), 4(-x), 2(x)$. The second data set is recorded with phase ϕ_6 incremented by 180° [i.e., $\phi_6 = 16(-x), 16(-y)$] and Acq = $2(x), 4(-x), 4(x), 4(-x), 2(x), 2(-x), 4(x), 4(-x), 4(x), 2(-x)$. Data for $\phi_6 = \pm x$ are recorded in an interleaved manner, exactly analogous to the recording of the real and imaginary components of States data (*26*). Note that in this sequence, unlike previous sequences, a 32-step phase cycle is employed. The first 16 steps of the cycle are identical to the phase cycling used in sequences a–d. Superimposed on this basic cycle is an additional 2-step phase cycle which interchanges the paths by which the cosine- and sine-modulated t_2 signals are returned to observable magnetization. This eliminates quadrature artifacts that could otherwise appear due to the different relaxation rates associated with the two transfer paths. Phase ϕ_4 and the receiver phase are inverted for each t_2 increment.

$$\sin(2\pi J_{NC'}T)I_x\cos(\omega_N t_2) \quad \text{and}$$

$$-\sin(2\pi J_{NC'}T)I_y\sin(\omega_N t_2). \quad [15]$$

The process of addition and subtraction of the data restores the signal intensity to what is observed in the nongradient version of the experiment (see sequence a); however, the noise floor of the data set increases by $\sqrt{2}$. Thus, the overall S/N is reduced by a factor of $\sqrt{2}$ relative to data sets where quadrature is obtained by the method of States (*26*). At first glance this may seem paradoxical since the process of coherence-transfer selection by gradients selects for either N- or P-type signals but not both.

It thus might be argued that the S/N should decrease by a full factor of 2 using this approach. In fact, a comparison of 1D spectra from data sets recorded with the sequence in Fig. 1a, $\phi_3 = \phi_4 = x$ and with the sequence in Fig. 1c, $\phi_3 = x$, N-type selection, shows that the S/N in the 1D spectra do infact differ by a full factor of 2 when $t_2 = 0$ (prior to postacquisition processing of N- and P-type data). In con-

trast, a comparison of 1D spectra from the same data sets shows that for $t_2 = 0$, $\phi_3 = x$, $\phi_4 = y$ (sequence in Fig. 1a), there is no signal, while the S/N in the 1D spectrum recorded with the sequence in Fig. 1c, $\phi_3 = x$, P-type selection, is identical to what was observed in the block collected with N-type selection. This can be seen clearly by setting $t_2 = 0$ and comparing Eqs. [13] and [14] with Eqs. [3] and [4]. Since the transformed 3D data sets are obtained by combining real and imaginary ^{15}N components (sequences in Figs. 1a and 1b) or combining N- and P-type data (sequences in Figs. 1c, 1d, and 1e), it is necessary to consider the S/N in both real and imaginary components and both N- and P-type components when computing the sensitivities expected from the different approaches. Consideration of S/N ratios associated with individual 1D slices of multidimensional data sets before complete processing of the data can lead to misleading results.

Inspection of Eq. [15] shows that the "add" and "subtract" data sets are 90° out of phase. This can be seen by noting that at the beginning of the acquisition period, magnetization from the add data set is proportional to I_x while magnetization from the subtract data set is proportional to I_y. This situation is remedied by the application of a 90° zero-order phase correction to either the add or the subtract data during the postacquisition processing step. This approach for the generation of pure-absorption spectra from data where coherence-transfer selection is achieved with the use of gradient pulses is, apart from slight differences in postacquisition data manipulation, identical to the approach suggested by Davis *et al.* (*9*), Prestegard and co-workers (*10*), and Boyd *et al.* (*11*).

Sequence d. The density operators for the magnetization at positions a and b are as given for sequence c. Immediately after the simultaneous ^1H and ^{15}N 90° pulses at the end of the constant-time period and for $\phi_6 = \pm x$, the density operator is

$$\rho_c = (i/2)\sin(2\pi J_{NC'}T)\{2(N_x \pm iN_z) \times I_y\exp(-i\theta_1) - 2(N_x \mp iN_z)I_y\exp(i\theta_1)\}. \quad [16]$$

The density operator at this point consists of double- and zero-quantum magnetization (N_xI_y) as well as NH magnetization antiphase with respect to the directly coupled ^{15}N spin (N_zI_y). During the subsequent $2\tau_c = 1/(2J_{NH})$ period, the antiphase single-quantum magnetization is refocused to give

$$\rho_d = \sin(2\pi J_{NC'}T)\{-2N_xI_y\sin\theta_1 \pm I_x\cos\theta_1\}, \quad [17]$$

where $\theta_1 = \omega_N t_2 - \gamma_N B_1(z)\tau_1$ as before. Application of simultaneous ^1H and ^{15}N 90°_y pulses, followed by the next $2\tau_c$ refocusing period, gives

$$\rho_e = \sin(2\pi J_{NC'}T)\{-I_x\sin\theta_1 \pm I_z\cos\theta_1\}. \quad [18]$$

Immediately before acquisition, the magnetization is given by

$$\rho_f = \sin(2\pi J_{NC'}T)\{I_y\cos(\theta_1 - \theta_2) - I_x\sin(\theta_1 - \theta_2)\} \quad (\phi_6 = x)$$

$$\rho_f = \sin(2\pi J_{NC'}T)\{-I_y\cos(\theta_1 + \theta_2) - I_x\sin(\theta_1 + \theta_2)\} \quad (\phi_6 = -x), \quad [19]$$

where $\theta_2 = \gamma_H B_2(z)\tau_2$ and θ_1 is defined above. The signals obtained for $\phi_6 = \pm x$ are stored in separate memory locations. Note that in order to refocus magnetization, the sign of one of the gradients, g3 or g8, must be changed when ϕ_6 is incremented by 180°, with only a single relative orientation of these gradients resulting in the refocusing of magnetization for each value of ϕ_6. Equation [19] can be recast as

$$\rho_f(\phi_6 = \pm x) = \sin(2\pi J_{NC'}T)\{-I_x\sin(\omega_N t_2) \pm I_y\cos(\omega_N t_2)\}, \quad [20]$$

where gradients g3 and g8 are adjusted so that refocusing of magnetization has occurred.

For each t_2 value, the signals obtained with $\phi_6 = \pm x$ and stored separately are added and subtracted and restored in separate memory locations. This results in an effective data matrix with the add and subtract signals at the start of acquisition given by $-2\sin(2\pi J_{NC'}T)I_x\sin(\omega_N t_2)$ and $2\sin(2\pi J_{NC'}T)I_y\cos(\omega_N t_2)$, respectively. Note that a 90° zero-order phase correction must be applied to either the add or the subtract data sets since the signal from the former is proportional to I_x, while the signal associated with the latter is proportional to I_y at the start of acquisition. It should be noted that the effect of adding and subtracting the data stored separately increases the signal intensity by a factor of 2 with a concomitant increase in the noise floor by a factor of $\sqrt{2}$. Comparing the results of this sequence with sequence c shows that in the absence of relaxation and pulse imperfections, a sensitivity enhancement of as much as a factor of 2 can be expected. Moreover, relative to the nongradient, unenhanced experiment (sequence a), an enhancement of as much as a factor of $\sqrt{2}$ may be obtained.

Sequence e. A calculation similar to that given for sequence d shows that for $\phi_6 = \pm x$, the signal at the start of the detection period is given by

$$\sin(2\pi J_{NC'}T)\{-I_x\sin(\omega_N t_2) \mp I_y\cos(\omega_N t_2)\}. \quad [21]$$

The data are combined in the manner described for sequences c and d to give cross peaks with pure-absorption

lineshapes. A comparison of Eqs. [20] and [21] shows that the S/N expected in spectra recorded with either scheme d or e should be identical. This is not surprising given the fact that for both schemes the signal that is selected is phase modulated in t_2. Hence, the use of gradients in scheme d will not compromise the sensitivity since the complete phase-modulated signal can be selected with the right combination of gradients.

THE EFFECTS OF RELAXATION DURING THE τ_c REFOCUSING PERIODS FOR SEQUENCES d AND e

In the preceding discussion, the effects of relaxation on the signal intensities have been neglected. However, for spectra recorded on macromolecules, transverse relaxation of the various density elements during τ_c may, in many cases, be nonnegligible. Denoting the transverse relaxation times of double- and zero-quantum ^{15}N–NH coherence and of single-quantum NH coherence by T_{2MQ} and T_{2NH}, respectively, and assuming that the longitudinal relaxation time of the NH spin is much longer than the delay τ_c, a straightforward calculation shows that, for sequence d, immediately prior to acquisition the magnetization is given by

$$\begin{aligned}\rho_f(\phi_6 = x) &= A[\{0.5 + 0.5\exp(-2\tau_c/T_{2MQ})\} \\ &\quad \times \{I_y\cos(\theta_1 - \theta_2) - I_x\sin(\theta_1 - \theta_2)\} \\ &\quad + \{0.5 - 0.5\exp(-2\tau_c/T_{2MQ})\} \times \{I_y\cos(\theta_1 + \theta_2) \\ &\qquad + I_x\sin(\theta_1 + \theta_2)\}] \\ \rho_f(\phi_6 = -x) &= A[\{0.5 + 0.5\exp(-2\tau_c/T_{2MQ})\} \\ &\quad \times \{-I_y\cos(\theta_1 + \theta_2) - I_x\sin(\theta_1 + \theta_2)\} \\ &\quad - \{0.5 - 0.5\exp(-2\tau_c/T_{2MQ})\} \times \{I_y\cos(\theta_1 - \theta_2) \\ &\qquad - I_x\sin(\theta_1 - \theta_2)\}], \quad [22]\end{aligned}$$

where $A = \sin(2\pi J_{NC'}T)\exp(-2\tau_c/T_{2NH})$, $\theta_1 = \omega_N t_2 - \gamma_N B_1(z)\tau_1$, and $\theta_2 = \gamma_H B_2(z)\tau_2$. In the derivation of Eq. [22], it has been assumed that $\zeta \ll T_{2NH}$. For the case where $\phi_6 = x$ and $\gamma_N B_1(z)\tau_1 = -\gamma_H B_2(z)\tau_2$, the only terms that contribute to observable magnetization are

$$\begin{aligned}\rho(\phi_6 = x) &= A\{0.5 + 0.5\exp(-2\tau_c/T_{2MQ})\} \\ &\quad \times \{I_y\cos(\omega_N t_2) - I_x\sin(\omega_N t_2)\},\end{aligned}$$

while for $\phi_6 = -x$ and $\gamma_N B_1(z)\tau_1 = \gamma_H B_2(z)\tau_2$,

$$\begin{aligned}\rho(\phi_6 = -x) &= A\{0.5 + 0.5\exp(-2\tau_c/T_{2MQ})\} \\ &\quad \times \{-I_y\cos(\omega_N t_2) - I_x\sin(\omega_N t_2)\}. \quad [23]\end{aligned}$$

Taking the sum and difference of data collected with $\phi_6 = \pm x$ gives

$$\begin{aligned}\rho(\text{sum}) &= -A\{0.5 + 0.5\exp(-2\tau_c/T_{2MQ})\}2I_x\sin(\omega_N t_2), \\ \rho(\text{difference}) &= A\{0.5 + 0.5\exp(-2\tau_c/T_{2MQ})\}2I_y\cos(\omega_N t_2). \quad [24]\end{aligned}$$

Thus relaxation leads to an attenuation of the expected sensitivity gain but, in the case of the gradient experiment indicated in Fig. 1d, will not lead to any spectral artifacts such as quadrature images. In contrast, for sequence e, the effects of relaxation during τ_c can result in quadrature artifacts. A calculation similar to that given above shows that for sequence e, the sum and difference of data collected with $\phi_6 = \pm x$ gives, immediately prior to acquisition,

$$\begin{aligned}\rho(\text{sum}) &= -2\sin(2\pi J_{NC'}T)(f_1 - f_2)I_x\sin(\omega_N t_2), \\ \rho(\text{difference}) &= 2\sin(2\pi J_{NC'}T)(f_1 + f_2)I_y\cos(\omega_N t_2), \quad [25]\end{aligned}$$

where $f_1 = \exp(-2\tau_c/T_{2NH})\{0.5 + 0.5\exp(-2\tau_c/T_{2MQ})\}$ and $f_2 = \exp(-2\tau_c/T_{2NH})\{0.5 - 0.5\exp(-2\tau_c/T_{2MQ})\}$. The mismatch of sine and cosine terms will lead to the appearance of quadrature artifacts when the data are processed according to the method of States (*26*).

The differences associated with the gradient and nongradient versions of the enhanced experiments (sequences d and e) with regard to the effects of relaxation can be appreciated as follows. The signal detected in the enhanced sequences is modulated in t_2 by both $\cos(\omega_N t_2)$ and $\sin(\omega_N t_2)$ terms and the paths traversed by the cosine- and sine-modulated data during refocusing into observable proton magnetization differ. For large molecules, the relaxation rates associated with the different paths may not be equal, giving rise to cosine and sine terms which have different intensities. This results in data consisting of predominantly N-type signals with a small P-type component and vice versa, as is indicated mathematically in Eq. [22]. Since the gradients used in experiment d select either N- or P-type data, but not both, the small component of ^{15}N magnetization that would give rise to F_2 quadrature artifacts in the nongradient experiment is eliminated by the action of the gradients. For the nongradient experiment, the quadrature artifacts can be eliminated by superimposing on the normal phase cycle scheme a two-step cycle which inverts the paths that the $\cos(\omega_N t_2)$- and $\sin(\omega_N t_2)$-modulated signals take while refocusing into observable proton magnetization. The cycle that is employed is indicated in the legend to Fig. 1e.

RESULTS AND DISCUSSION

In order to verify the results described under Theory and quantitate the sensitivity gains that the enhanced sequences

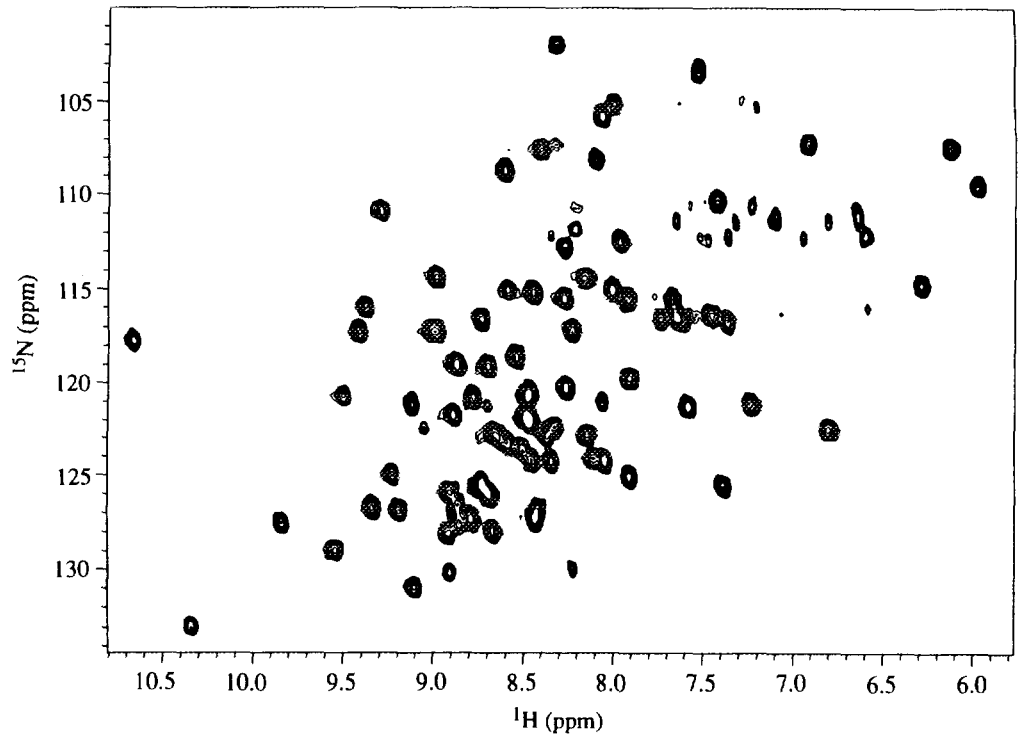

FIG. 2. Two-dimensional contour plot of the pure-absorption $^{1}H-^{15}N$ spectrum of CBD, 2 mM in 90% H_2O, 10% D_2O, pH 7.0, 30°C, recorded at 500 MHz on a Varian UNITY spectrometer equipped with a triple-resonance gradient probehead and a gradient amplifier unit. The spectrum was obtained with the sequence in Fig. 1d with $t_1 = 0$ and $\phi_3 = x$. The data set was recorded with 48 complex ^{15}N points and 32 scans per FID and a relaxation delay of 1 s, giving rise to a total acquisition time of approximately one hour.

can provide, we have measured the S/N ratios of a large number of cross peaks in 2D $^{1}H-^{15}N$ maps of a number of different proteins. The 2D spectra were generated using the sequences in Fig. 1 with $t_1 = 0$ and $\phi_3 = x$. Because S/N ratios of cross peaks from different experiments are compared, we have used the same basic 16-step phase cycle in each sequence. For the gradient experiments, however, it is clear that the phase cycling could be reduced drastically through the use of pulsed field gradients, as has recently been described by Bax and Pochapsky in connection with the

TABLE 1
Average S/N Ratios of HNCO Pulse Schemes Considered[a]

Protein	A	B	C	D	E	F
Protein S fragment[b]	65	0.87 ± 0.13	0.56 ± 0.06	0.75 ± 0.10	1.26 ± 0.16	1.22 ± 0.17
CBD[c]	73	0.70 ± 0.11	0.53 ± 0.06	0.71 ± 0.07	1.18 ± 0.21	1.20 ± 0.12
Calmodulin[d]	92	0.87 ± 0.13	0.56 ± 0.06	0.76 ± 0.10	1.24 ± 0.14	1.24 ± 0.16
Protein S[e]	106	0.81 ± 0.16	0.53 ± 0.10	0.73 ± 0.12	1.14 ± 0.19	1.16 ± 0.15

Notes. A, number of cross peaks averaged; B, experiment in Fig. 1a with water suppression achieved by a combination of a 30 Hz field applied for 1 s prior to the start of sequence as well as the x, y purge scheme described in the text; C, experiment in Fig. 1b; D, experiment in Fig. 1c; E, experiment in Fig. 1d; F, experiment in Fig. 1e.

[a] S/N values are relative to the values obtained using the sequence in Fig. 1a, where water suppression is achieved using the purge scheme described in the text. $S/N = 1/n\ \Sigma\ (S_k/N)_i/(S_k/N)_j$, where $(S_k/N)_i$ is the S/N of peak k in experiment i and n is the number of peaks that the summation includes. Experiment j is the experiment in Fig. 1a with water suppression achieved via the purge scheme only (no presaturation).

[b] The protein concentration is 1.5 mM, 0.1 M KCl, 95% H_2O, 5% D_2O, pH = 6.4, T = 30°C (93 amino acids).

[c] The protein concentration is 2.0 mM, 90% H_2O, 10% D_2O, pH 7.0, T = 30°C (dimer of 110 amino acids/monomer).

[d] The protein concentration is 1.5 mM, 0.1 M KCl, 95% H_2O, 5% D_2O, pH 6.2, T = 50°C (148 amino acids). Identical results were obtained at T = 30°C.

[e] The protein concentration is 1.5 mM, 0.1 M KCl, 95% H_2O, 5% D_2O, pH 6.7, T = 30°C (173 amino acids).

HN(CO)CA experiment (*23*). Figure 2 shows a 2D ^1H–^{15}N correlation map of 2 m*M C. fimi* CBD (dimer of 110 amino acids/monomer) obtained with the sequence in Fig. 1d. The spectrum was recorded at 500 MHz on a Varian UNITY spectrometer equipped with a triple-resonance gradient probehead and a gradient amplifier unit. Other proteins that have been examined include *X. laevis* calmodulin (148 amino acids), *M. xanthus* protein S (173 amino acids), and a 93-amino acid fragment of protein S. Table 1 lists the average S/N ratios of cross peaks in the various experiments relative to the experiment in Fig. 1a [water suppression via x, y purge pulses (*27*) exclusively] for the proteins examined. Cross-peak volumes were obtained using a surface-fitting routine (NMRi software). The average rms noise in each spectrum was calculated using a simple program written in house. The S/N of each experiment relative to the experiment in Fig. 1a is calculated as $S/N = 1/n \sum_k (S_k/N)_i/(S_k/N)_j$, where $(S_k/N)_i$ is the signal-to-noise of peak k measured in experiment i, n is the number of peaks included in the summation, and j is the experiment in Fig. 1a with water suppression achieved via the purge pulses only. In order to increase the number of cross peaks that could be surface fitted, the resolution in each spectrum was improved by doubling the number of ^{15}N time-domain points using linear prediction. A comparison of relative S/N ratios $[1/n \sum_k (S_k/N)_i/(S_k/N)_j]$ calculated from spectra processed with and without linear prediction showed that linear prediction did not change the measured ratios.

The experimental results indicated in Table 1 confirm the conclusions predicted under Theory. The use of gradients to select for ^{15}N magnetization during nonevolution delays (Fig. 1b) results in a full factor of 2 sensitivity loss relative to spectra obtained with the sequence in Fig. 1a and with water suppression achieved via x, y purge pulses. A factor of 2 loss in S/N is intolerable in many applications. The gradient scheme in Fig. 1c, in which one of the gradients used to select for ^{15}N magnetization is applied during the ^{15}N evolution delay, gives rise to N- and P-type phase-modulated signals which are stored separately. Following postacquisition processing, described previously, pure-absorption spectra are obtained having S/N that is $\sqrt{2}$ lower than that of spectra generated by the method of States (*26*). This is indicated clearly in Table 1. In contrast, the enhanced-sensitivity gradient experiment in Fig. 1d, with gradient selection of ^{15}N magnetization, does not suffer any sensitivity losses relative to States data sets for the proteins considered here. In fact, sensitivity gains of as much as a factor of $\sqrt{2}$ can, in principle, be obtained. In practice it is unlikely that such gains will be fully recognized due to the increased number of pulses and delays in the enhanced sequences. Nevertheless, sensitivity enhancements of ~25% are obtained for the case of a 93-amino acid fragment of protein S, while enhancements of ~15% are observed for protein S (173 amino acids). Since most of the proteins studied in NMR laboratories to date are smaller in size than ~200 amino acids, it is anticipated that the gradient approach suggested here will result in spectra having noticeable sensitivity gains over spectra recorded with the triple-resonance schemes currently in use. We have also recorded nongradient enhanced HNCO spectra in order to determine whether the use of gradients results in any deleterious effects on sensitivity. The results from these experiments are listed in Table 1. A comparison of results obtained for the gradient and nongradient versions of the enhanced-sensitivity experiments (Figs. 1d and 1e) using Student's t test (*27*) indicates that at the 95% confidence level there is no difference between the S/N values measured in either experiments. However, there is far better suppression

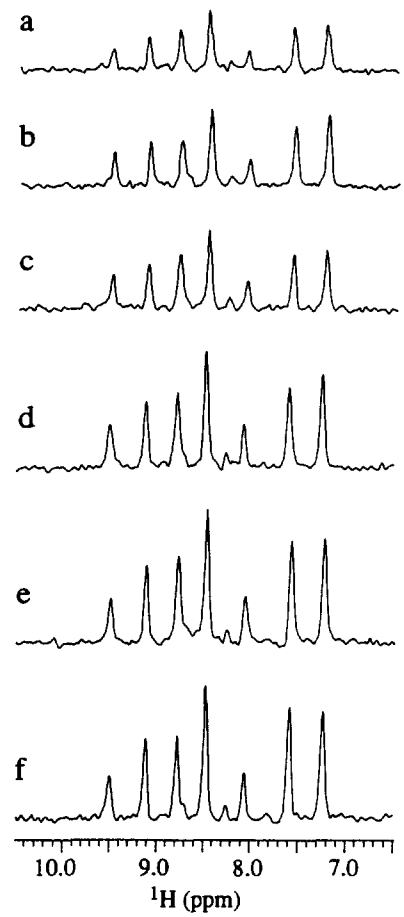

FIG. 3. Cross sections from 2D ^1H–^{15}N spectra of CBD recorded with the sequences in Fig. 1 with $t_1 = 0$, $\phi_3 = x$. All cross sections are at a ^{15}N chemical shift of 120.8 ppm and are normalized so that the noise level is the same in each spectrum: (a) sequence in Fig. 1b with water suppression achieved via the pulsed field gradients; (b) sequence in Fig. 1a with water suppression achieved via the use of a 30 Hz presaturation field for 1 s as well as the x, y purge pulses; (c) sequence in Fig. 1c with water suppression achieved via field gradients; (d) sequence in Fig. 1a with water suppression achieved via the x, y purge pulses. No presaturation was applied: (e) sequence in Fig. 1e with water suppression achieved via the x, y purge pulses; (f) sequence in Fig. 1d with water suppression achieved via the pulsed field gradients.

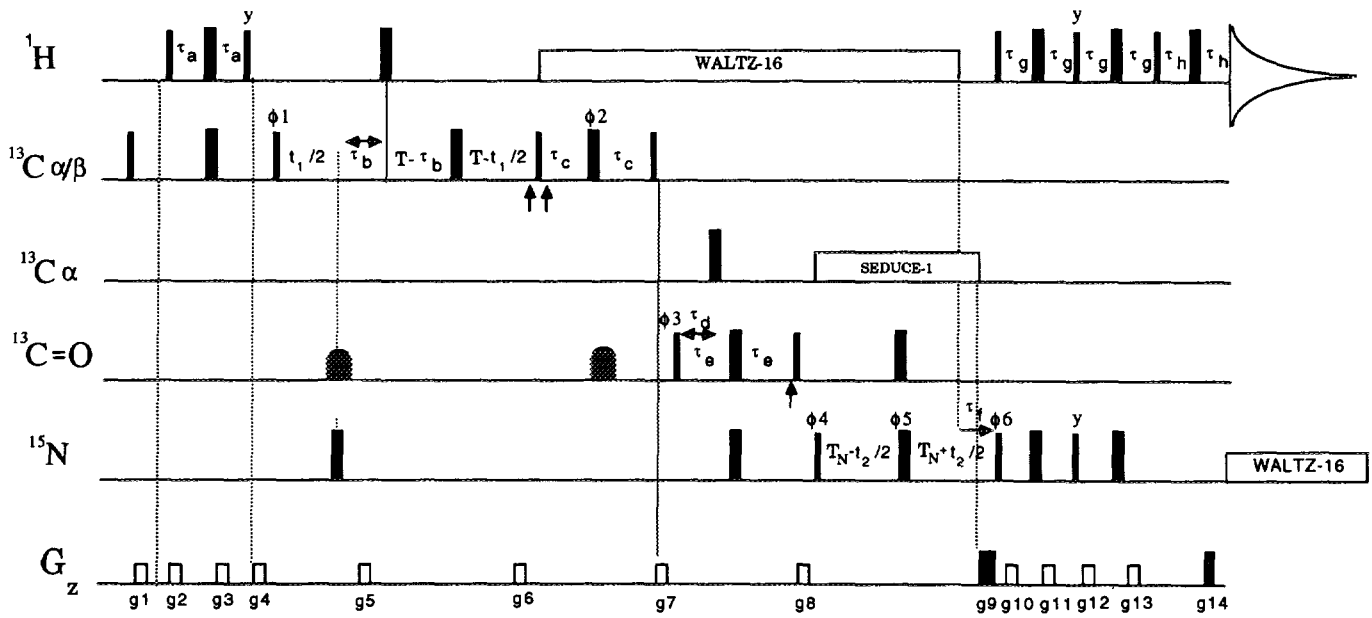

FIG. 4. Pulse sequence of the enhanced gradient CBCA(CO)NH sequence (*16*). The values of τ_a, τ_c, τ_d, τ_e, τ_f, τ_g, τ_h, T_N, and T are set to 1.8 ms, 3.6 ms, 4.4 ms, 12.4 ms, 5.5 ms, 2.3 ms, 300 μs, 12.4 ms, and 3.6 ms, respectively. The value of τ_b is chosen such that $2\tau_b + 2\delta_{C'} + \delta_N = 0.3/J_{HC} \sim 2.2$ ms, where $\delta_{C'}$ and δ_N are the shaped C′ 180° and ^{15}N 180° pulse widths (the C′ and ^{15}N 180° pulses are applied sequentially). WALTZ decoupling (*30*) is achieved using a 6.3 kHz field on the ^{1}H channel and a 1 kHz field on the ^{15}N channel. SEDUCE-1 decoupling (*24, 25*), centered at 54 ppm, using a 825 Hz field ensures that ^{15}N magnetization does not evolve due to scalar coupling to ^{13}Cα during the constant-time t_2 evolution period. The SEDUCE decoupling is terminated prior to the application of gradient pulse g9. The ^{13}Cα/β pulses are applied at 43 ppm, the ^{13}Cα pulses are centered at 54 ppm, and the C′ pulses are applied as phase-modulated pulses with the center of excitation at 175 ppm. All C′ rectangular pulses are applied at a field strength of 4.0 kHz. The shaped C′ 180° pulses (250 μs) are applied using a shape profile given by a 180° element in the SEDUCE-1 decoupling scheme. The ^{13}Cα/β 90° and 180° pulses are applied at field strengths of 4.4 and 9.8 kHz, while the ^{13}Cα 180° pulse is applied at a strength of 9.0 kHz. The ^{13}Cα/β (^{13}Cα) pulse widths and C′ pulse widths used ensure a minimal perturbation of the C′ and ^{13}Cα/β (^{13}Cα) spins, respectively (*19*). The first two arrows in the sequence indicate the position of application of the C′ 180° pulses to compensate for the Bloch–Siegert effects of the shaped C′ 180° pulses indicated in the sequence (*20, 25, 32*). The second shaped C′ 180° pulse is applied after the ^{13}Cα/β 180° pulse of phase ϕ_2. Thus, the Bloch–Siegert compensation pulse must be applied immediately after the ^{13}Cα/β 90° pulse at the start of the delay of duration $2\tau_c$. The third arrow indicates the position where an additional ^{13}Cα 180° pulse is applied to compensate for the Bloch–Siegert shift introduced by the ^{13}Cα 180° pulse applied τ_d after the C′ 90° pulse of phase ϕ_3. The phase cycling employed is $\phi_1 = x$; $\phi_2 = x, -x$; $\phi_3 = x, -x$; $\phi_4 = x$; $\phi_5 = 2(x), 2(-x)$; Acq = $x, -x$. Quadrature in F_1 is obtained via States–TPPI of ϕ_1 (*31*). For each t_2 value, FIDs are recorded with $\phi_6 = x$ and $\phi_6 = -x$. These FIDs are stored separately, in a manner analogous to the way in which cosine- and sine-modulated t_2 components are stored. When ϕ_6 is inverted, the sign of g14 is also inverted. For each t_2 value, data from $\phi_6 = x$ and $\phi_6 = -x$ are combined as described in the text to yield pure-absorption lineshapes in the ^{15}N dimension. Phase ϕ_4 and the receiver phase are inverted each time t_2 is incremented. The duration and strengths of the gradients are g1 = g2 = g3 = g10 = g11 = g12 = g13 = (500 μs, 8 G/cm); g4 = (1 ms, 20 G/cm); g5 = g6 = (250 μs, 20 G/cm); g7 = (1 ms, 15 G/cm); g8 = (1.5 ms, 20 G/cm); g9 = (2.5 ms, 30 G/cm); g14 = (250 μs, ±29.04 G/cm). The gradients are inserted in the sequence in such a way as to leave the maximum amount of time between the application of a gradient and the subsequent application of an RF pulse. For example, although in principle g2 could be inserted anywhere within the first τ_a delay, the insertion of g2 immediately following the first ^{1}H 90° pulse ensures that residual effects of the gradient are minimized before the application of the ^{1}H/^{13}C$_{\alpha/\beta}$ 180° pulse pair. We have found that a delay of 50 μs between the application of gradient and RF pulses is a sufficient recovery time in any of the applications that we have considered to date, although this value will clearly vary between systems and in a manner dependant on the strength and duration of gradient pulses used. Coherent decoupling is interrupted during the application of gradients g7, g8, and g9.

of water in the gradient experiment, a potential reduction in the number of artifacts, and the possibility of significantly reducing the number of phase-cycling steps relative to non-gradient experiments (*23*). The differences in sensitivity associated with the experiments in Fig. 1 are illustrated in Fig. 3, where cross sections at an ^{15}N chemical shift of 120.8 ppm from 2D spectra recorded on CBD are shown.

Close examination of Table 1 shows that the use of presaturation can give rise to a significant reduction in the sensitivity of cross peaks in triple-resonance data sets. This was noted previously in a comparison of signal intensities in HSQC spectra of CBD recorded with and without presaturation (*12*). The attenuation varies from as much as a factor of 1.4 in the case of CBD to a factor of 1.1 for calmodulin and the 93-amino acid fragment of protein S. The large reduction in sensitivity due to presaturation in the case of CBD relative to the other proteins is, at least in part, due to the higher pH (7.0) of the sample. However, the loss in sensitivity in all cases suggests that presaturation should be avoided if possible. We have found that an efficient scheme for water suppression is one in which a 10 kHz purge pulse is applied for approximately 6 ms along x followed by the application

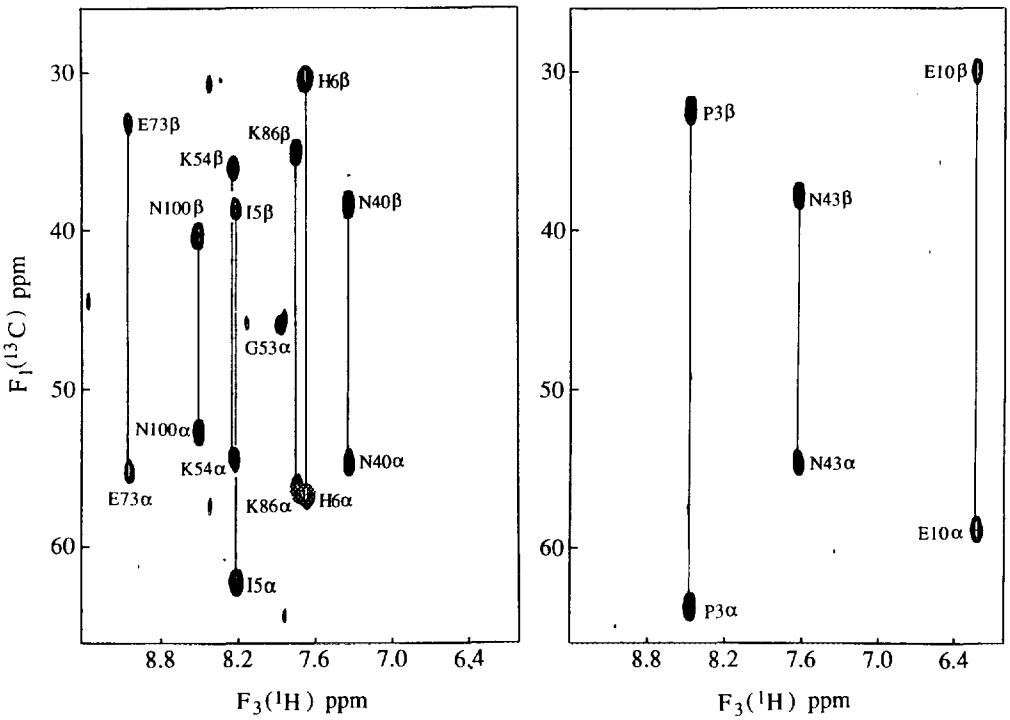

FIG. 5. Sections of slices (F_1/F_3) from the CBCA(CO)NH experiment at ^{15}N shifts of 109.33 ppm (right) and 120.02 ppm (left). Many of the cross peaks show greater intensity on adjacent slices. The experiment was recorded on a 2.5 mM sample of PLC-γ SH2 (c-terminal fragment) at 500 MHz, 30°C, pH 6.2. The spectrum was recorded as a 60 × 32 × 512 complex matrix. The final size of the transformed absorptive matrix, including linear prediction of the t_2 time domain, was 128 × 128 × 512.

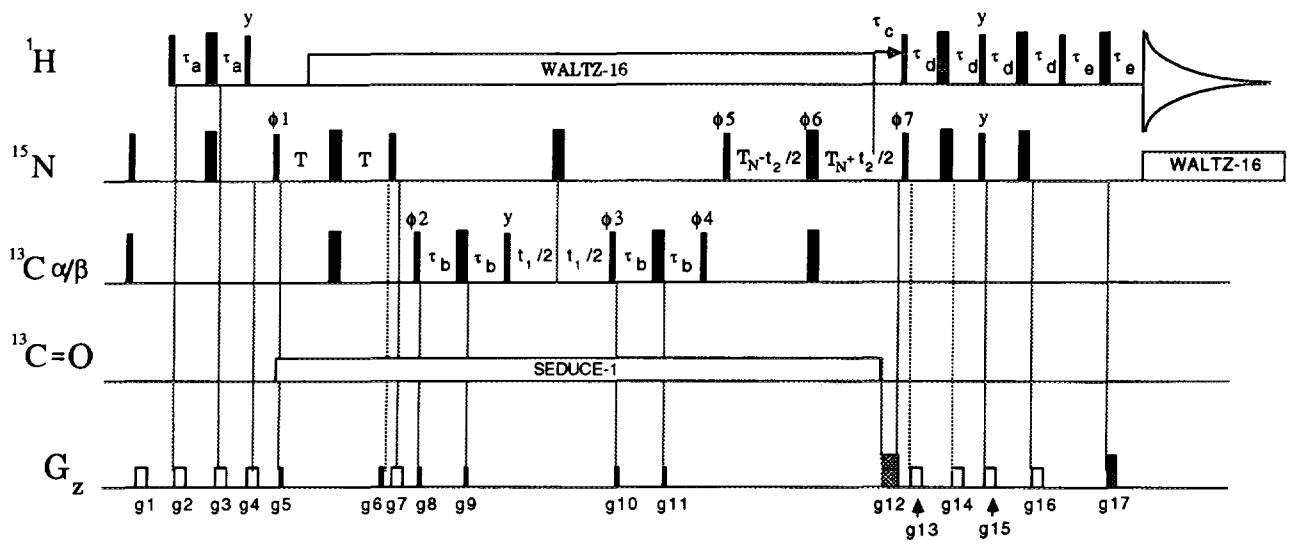

FIG. 6. Pulse sequence of the enhanced gradient HNCACB sequence (*17*). The values of τ_a, τ_b, τ_c, τ_d, τ_e, T_N, and T are set to 2.3, 3.5, 5.5, 2.3, 0.3, 12.4, and 12.4 ms, respectively. All $^{13}C\alpha/\beta$ pulses are centered at 43 ppm and applied at a field strength of 18.5 kHz. Carbonyl decoupling is achieved using a 600 Hz SEDUCE-1 decoupling scheme (*24, 25*) centered at 175 ppm. WALTZ decoupling was achieved using a ^1H field of 6.3 kHz and a ^{15}N field of 1 kHz. Decoupling is terminated prior to the application of a gradient pulse, as discussed in the text. The phase cycling employed is $\phi_1 = x, -x$; $\phi_2 = 2(x), 2(-x)$; $\phi_3 = y$; $\phi_4 = x$; $\phi_5 = x$; $\phi_6 = 4(x), 4(-x)$; $\phi_7 = x$; Acq = $x, -x, -x, x$. Quadrature in F_1 is obtained by incrementing both of phases ϕ_3 and ϕ_4 simultaneously by 90°. Phase ϕ_4 is incremented by 180° along with the phase of the receiver for each successive complex t_1 point. For each t_2 value, FIDs are recorded with $\phi_7 = x$ and $\phi_7 = -x$. The sign of gradient g17 is inverted when ϕ_7 is incremented by 180°. Phase ϕ_5 and the receiver phase are incremented by 180° for each successive complex t_2 point. The duration and strengths of the gradients are g1 = (0.5 ms, 8 G/cm); g2 = g3 = (0.5 ms, 4 G/cm); g4 = (1.0 ms, 10 G/cm); g5 = g6 = (100 μs, 10 G/cm); g7 = (0.5 ms, 8 G/cm); g8 = g9 = (100 μs, 10 G/cm); g10 = g11 = (100 μs, 7 G/cm); g12 = (2.5 ms, 30 G/cm); g13 = g14 = g15 = g16 = (0.5 ms, 8 G/cm); g17 = (250 μs, ±29.08 G/cm). Gradient g17 was optimized by maximizing the signal as a function of the gradient strength. Coherent decoupling is interrupted during the application of gradients g6–g12.

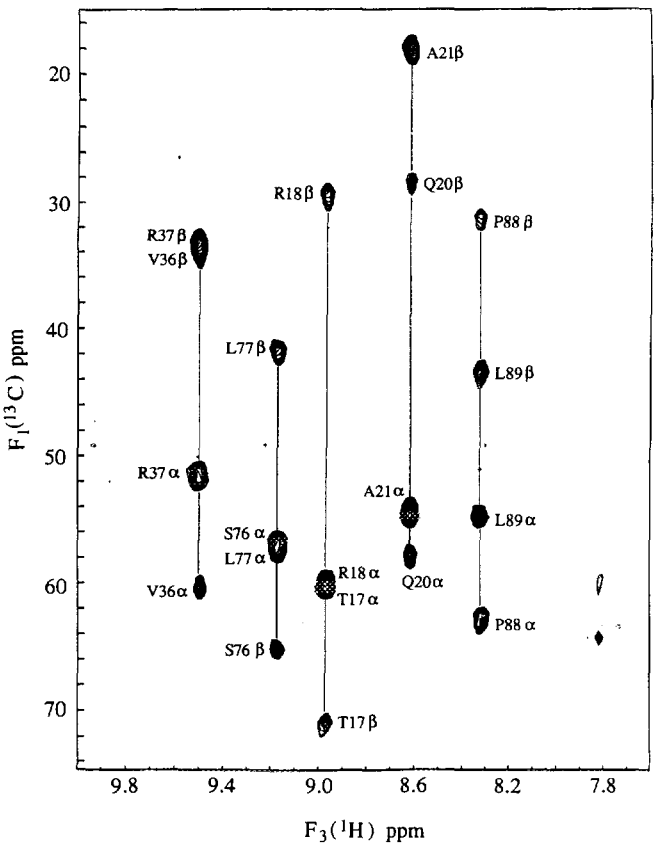

FIG. 7. Slice (F_1/F_3) from the HNCACB experiment at an ^{15}N shift of 122.82 ppm. The experiment was recorded on a 1.5 m*M* sample of PLC-γSH2 (c-terminal fragment) complexed with a 12-amino acid peptide from PDGFR at 500 MHz, 30°C, pH 6.2. The spectrum was recorded as a 32 × 36 × 512 complex matrix. Prior to processing in the $^{13}C\alpha/\beta$ dimension, the data were multiplied by a function of the form $\cos^{-1}(\pi J t_1)$, with J = 37 Hz, to remove the effect of the Cα–Cβ homonuclear coupling (*17*). The final size of the transformed absorptive matrix, including linear prediction of the t_2 time domain, was 64 × 128 × 512. Negative peaks are indicated with broken line contours.

of a 3.5 ms *y* purge pulse. The purge pulses are applied during a period in the sequence when the magnetization of interest does not involve ^1H spins and is along the *z* axis. When this situation occurs in a number of places in the pulse scheme, the purge pulses are inserted as close to the detection period as possible. In the HNCO nongradient sequences considered in Fig. 1, the purge pulses are applied when magnetization is of the form $2N_zC'_z$. Note that at this point the magnetization is longitudinal, so that the operative relaxation times are related to the ^{15}N and $^{13}C'$ T_1, and that no ^1H magnetization of interest is present.

Figure 4 shows the gradient enhanced version of the CBCA(CO)NH pulse sequence developed by Grzesiek and Bax (*16*). Gradients are employed both to reduce the number of phase-cycling steps in the sequence and to select for ^{15}N magnetization. The details of the magnetization-transfer scheme in this experiment have been described previously (*16*) and will not be elaborated on here. It is worthwhile, however, to discuss the use of the gradients in this experiment. In order to ensure that magnetization originates on ^1H and not ^{13}C, carbon magnetization is completely randomized at the start of the experiment by the application of a ^{13}C 90° pulse followed by a field gradient (*8*). In nongradient applications, the elimination of signals originating from ^{13}C magnetization is achieved by inverting the phase of the first (or second) ^1H 90° pulse and the phase of the receiver in alternate scans. As discussed by Bax and Pochapsky (*23*), the application of gradients of equal strength and duration on opposite sides of a 180° refocusing pulse ensures that only those terms are retained that have a transverse operator before and after the pulse. Gradient pulse pairs g2 and g3, g5 and g6, g10 and g11, and g12 and g13 ensure, for example, that transverse magnetization before the refocusing pulse is not transferred into *z* magnetization after the pulse. In addition, any transverse magnetization that does not experience the effects of the refocusing pulse is completely eliminated by the action of the gradients. Gradient pulses g4, g7, and g8 are applied when the magnetization of interest is of the form A_zB_z, where A_z and B_z are the *z* components of magnetization of spins A and B, respectively. This magnetization is not affected by the action of the gradients, while any transverse magnetization components present at this time that could give rise to spectral artifacts are eliminated. Gradients g9 and g14 are tuned to select for magnetization that passes through ^{15}N. The use of these two gradients also provides excellent water suppression.

The combined use of the gradient pulses described above leads to a considerable decrease in the number of phase-cycling steps. At first glance it may appear possible to reduce the phase cycling still further by eliminating the phase-cycling steps ϕ_2 and ϕ_5 and inserting gradient pulse pairs on either sides of the corresponding 180° pulses. For the case of the 180° $^{13}C\alpha/\beta$ pulse of phase ϕ_2, this would require the insertion of the gradient pulse pair during the τ_c periods. However, the application of a gradient pulse pair during this time could well interfere with the efficiency of ^1H decoupling, used to maximize sensitivity in the experiment by maintaining carbon magnetization in phase (*20, 29*). Off-resonance decoupling effects would be significant if the effective field generated by the gradient pulses exceeds the bandwidth of the decoupling sequence. The resultant signal, which is the sum over the entire sample volume, can be greatly decreased. A similar situation exists during the constant-time ^{15}N evolution period. Thus, if gradients are to be inserted during these periods, it is necessary to terminate decoupling prior to the application of the gradient pulse(s) and to limit the time of application of the gradient(s) so that significant antiphase magnetization does not build up. The approach that we favor with regard to the use of gradients to minimize phase cycling is to employ gradients whenever their use does not compromise the sensitivity of the experiment in question.

Therefore the use of coherent ^1H decoupling to prevent the evolution of antiphase heteronuclear magnetization during the course of this experiment is retained, at the expense of the use of a very modest phase cycle.

The gradient enhanced CBCA(CO)NH sequence is illustrated on a sample of 2.5 m*M* PLC-γ SH2 fragment (106 amino acids), 0.1 *M* Na_3PO_4, pH 6.2, 90% H_2O, 10% D_2O, 30°C. The spectrum was obtained from a 60 × 32 × 512 complex matrix with acquisition times of 6.6 ms (t_1), 19.4 ms (t_2), and 64.0 ms (t_3). Sixteen scans were recorded with a repetition delay of 1.0 s, giving rise to a total acquisition time of approximately 32 hours. Figure 5 shows two slices from the enhanced CBCA(CO)NH spectrum at ^{15}N shifts of 109.3 and 120.0 ppm.

Figure 6 shows the gradient enhanced version of the HNCACB experiment (*17*). The use of gradients in this sequence and in the sequence in Fig. 4 is essentially identical. In this particular sequence, it is especially important to eliminate artifacts arising from imperfections in the $^{13}C\alpha/\beta$ 180° pulses applied in the middle of the τ_b periods. For this reason, very short (100 μs) gradient pulses are inserted on both sides of these $^{13}C\alpha/\beta$ 180° pulses and during their application coherent decoupling is stopped.

Figure 7 illustrates a slice from the enhanced HNCACB experiment at an ^{15}N chemical shift of 122.8 ppm. The sample used for this experiment was a 1.5 m*M* PLC-γ SH2 fragment complexed with a 12-amino acid fragment comprising the high-affinity binding site from platelet-derived growth factor receptor (PDGFR), 0.1 *M* Na_3PO_4, pH 6.2, 90% H_2O, 10% D_2O, 30°C. The spectrum was recorded as a 32 × 36 × 512 complex matrix with acquisition times of 4.2 ms (t_1), 21.8 ms (t_2), and 64 ms (t_3). A 1.0 s repetition delay and 32 scans were recorded to give a total acquisition time of approximately 42 hours. The spectrum is phased so that the $C\alpha(\beta)$ resonances are positive (negative).

In the CBCA(CO)NH and HNCACB sequences, as well as in the HNCO schemes discussed above, carbon magnetization is not selected by gradient pulses since, in the absence of a scheme to enhance sensitivity, the use of gradients to select for carbon magnetization in these experiments does result in a loss in sensitivity. The use of a sensitivity-enhancement scheme, such as is employed in the case where ^{15}N magnetization is selected by gradients (Fig. 1d), seems likely to be impractical for the selection of ^{13}C magnetization in the present pulse sequences in part due to the small size of the couplings involved, the carbon–carbon couplings present, and the increased number of pulses and delays that such an approach would require. In addition, it must be kept in mind that using this approach, enhanced sensitivity is possible only for magnetization from heteronuclei that are part of AX spin systems (*14*).

It is straightforward to incorporate the enhanced-sensitivity approach into the framework of all triple-resonance NH experiments. A comparison of the CBCA(CO)NH sequence of Grzesiek and Bax (*16*) or the HNCACB sequence of Wittekind and Mueller (*17*) with the enhanced gradient versions of the CBCA(CO)NH and HNCACB sequences presented here shows how this can be done and also illustrates the decrease in the number of phase-cycling steps that is made possible with the use of gradients.

In summary, in this paper, a number of different HNCO triple-resonance experiments have been compared. It has been shown that for the proteins considered in this study, with molecular weights ranging from ~10 to 20 kDa, the enhanced gradient sequence with gradient selection of ^{15}N magnetization is as sensitive as its nongradient enhanced counterpart and is more sensitive than any of the other schemes considered. The use of gradients in triple-resonance experiments greatly improves water suppression, allows for a minimal phase cycle, and reduces artifacts. Given these benefits and the fact that sensitivity is not compromised, it seems likely that the enhanced gradient triple-resonance experiments are to be preferred over their nongradient counterparts for application to many protein systems currently studied by triple-resonance NMR.

ACKNOWLEDGMENTS

The authors are grateful to Dr. Mitsu Ikura (Ontario Cancer Institute) for kindly making available a number of ^{15}N,^{13}C samples used in this study and to Dr. Julie Forman-Kay and Mr. Alex Singer, Hospital for Sick Children, Toronto, for making available the assignments for PLC-γ SH2 prior to publication. Valuable discussions with Drs. Luciano Mueller (Bristol-Myers Squibb) and Mark Rance (Scripps Research Institute) are gratefully acknowledged. This research was supported by grants from the Natural Sciences and Engineering Research Council of Canada and the National Cancer Institute of Canada.

Note added in proof. In present applications, the gradients used to select the appropriate coherence-transfer pathway (for example, g3 and g8 in Fig. 1d, g9 and g14 in Fig. 4, and g12 and g17 in Fig. 6) are applied for 1.25 ms (^{15}N) and 125 μs (^1H) and the delay ξ (Fig. 1d), τ_h (Fig. 4), and τ_c (Fig. 6) are set to 500 μs. Very recently work of a similar nature has been published by Schleucher *et al.* (J. Schleucher, M. Sattler, and C. Griesinger, *Angew. Chem. Int. Ed. Engl.* **10**, 32, 1993).

REFERENCES

1. A. Bax, P. G. De Jong, A. F. Mehlkopf, and J. Smidt, *Chem. Phys. Lett.* **69,** 567 (1980).
2. A. A. Maudsley, A. Wokaun, and R. R. Ernst, *Chem. Phys. Lett.* **55,** 9 (1978).
3. R. E. Hurd and B. K. John, *J. Magn. Reson.* **92,** 658 (1991).
4. G. W. Vuister, R. Boelens, R. Kaptein, R. E. Hurd, B. John, and P. C. M. Van Zijl, *J. Am. Chem. Soc.* **113,** 9688 (1991).
5. G. W. Vuister, R. Boelens, R. Kaptein, M. Burgering, and P. C. M. Van Zijl, *J. Biomol. NMR* **2,** 301 (1992).
6. B. K. John, D. Plant, P. Webb, and R. E. Hurd, *J. Magn. Reson.* **98,** 200 (1992).
7. R. E. Hurd, B. K. John, and H. D. Plant, *J. Magn. Reson.* **93,** 666 (1991).
8. L. E. Kay, *J. Am. Chem. Soc.* **115,** 2055 (1993); L. E. Kay, G. Y. Xu, A. U. Singer, D. R. Muhandiram, and J. D. Forman-Kay, *J. Magn. Reson. B* **101,** 333 (1993).

9. A. L. Davis, J. Keeler, E. D. Laue, and D. Moskau, *J. Magn. Reson.* **98,** 207 (1992).
10. J. R. Tolman, J. Chung, and J. H. Prestegard, *J. Magn. Reson.* **98,** 462 (1992).
11. J. Boyd, N. Soffe, B. K. John, D. Plant, and R. Hurd, *J. Magn. Reson.* **98,** 660 (1992).
12. L. E. Kay, P. Keifer, and T. Saarinen, *J. Am. Chem. Soc.* **114,** 10663 (1992).
13. J. Cavanagh, A. G. Palmer, P. E. Wright, and M. Rance, *J. Magn. Reson.* **91,** 429 (1991).
14. A. G. Palmer, J. Cavanagh, P. E. Wright, and M. Rance, *J. Magn. Reson.* **93,** 151 (1991).
15. A. G. Palmer, J. Cavanagh, R. A. Byrd, and M. Rance, *J. Magn. Reson.* **96,** 416 (1992).
16. S. Grzesiek and A. Bax, *J. Am. Chem. Soc.* **114,** 6291 (1992).
17. M. Wittekind and L. Mueller, *J. Magn. Reson. B* **101,** 201 (1993).
18. M. Ikura, L. E. Kay, and A. Bax, *Biochemistry* **29,** 4659 (1990).
19. L. E. Kay, M. Ikura, R. Tschudin, and A. Bax, *J. Magn. Reson.* **89,** 496 (1990).
20. S. Grzesiek and A. Bax, *J. Magn. Reson.* **96,** 432 (1992).
21. A. L. Davis, R. Boelens, and R. Kaptein, *J. Biomol. NMR* **2,** 395 (1992).
22. O. W. Sørensen, G. W. Eich, M. H. Levitt, G. Bodenhausen, and R. R. Ernst, *Prog. NMR Spectrosc.* **16,** 163 (1983).
23. A. Bax and S. Pochapsky, *J. Magn. Reson.* **99,** 638 (1992).
24. M. A. McCoy and L. Mueller, *J. Am. Chem. Soc.* **114,** 2108 (1992).
25. M. A. McCoy and L. Mueller, *J. Magn. Reson.* **98,** 674 (1992).
26. D. J. States, R. A. Haberkorn, and D. J. Ruben, *J. Magn. Reson.* **48,** 286 (1982).
27. B. A. Messerle, G. Wider, G. Otting, C. Weber, and K. Wüthrich, *J. Magn. Reson.* **85,** 608 (1989).
28. Z. H. Zar, "Biostatistical Analysis," 2nd ed., Prentice-Hall, Englewood Cliffs, New Jersey, 1984.
29. B. T. Farmer II, R. A. Venters, L. D. Spicer, M. G. Wittekind, and L. Mueller, *J. Biomol. NMR* **2,** 195 (1992).
30. A. J. Shaka, J. Keeler, T. Frenkiel, and R. Freeman, *J. Magn. Reson.* **52,** 335 (1983).
31. D. Marion, M. Ikura, R. Tschudin, and A. Bax, *J. Magn. Reson.* **85,** 393 (1989).
32. G. W. Vuister and A. Bax, *J. Magn. Reson.* **98,** 428 (1992).